Zhou *et al. Journal of Nanobiotechnology* (2025) 23:137
https://doi.org/10.1186/s12951-025-03186-4

Journal of Nanobiotechnology

RESEARCH **Open Access**

Zinc-copper bimetallic nanoplatforms trigger photothermal-amplified cuproptosis and cGAS-STING activation for enhancing triple-negative breast cancer immunotherapy

Bangyi Zhou[1,2†], Mengyao Chen[1,2†], Zhixing Hao[1†], Lili Li[1,2], Yixin Zhang[1,2], Baoru Fang[3], Miner Shao[1,2], Guohong Ren[1,4], Ke Wang[3], Huiying Liu[1,2], Jingxuan Zhu[1,2], Xinyi Zhang[1,2], Shuyan Yuan[1,2], I Sitou[1,2], Jing Zhao[1,2], Jian Huang[1,4*], Zhangsen Yu[3*] and Fuming Qiu[1,2*]

Abstract
Triple-negative breast cancer (TNBC) is characterized by high rates of metastasis and recurrence, along with a low sensitivity to immunotherapy, resulting in a paucity of effective therapeutic strategies. Herein, we have developed polydopamine-coated zinc-copper bimetallic nanoplatforms (Cu-ZnO$_2$@PDA nanoplatforms, abbreviated CZP NPs) that can efficiently induce photothermal amplified cuproptosis and cGAS-STING signaling pathway activation, thereby reversing the immunosuppressive tumor microenvironment of TNBC, upregulating PD-L1 expression, and boosting the efficacy of anti-programmed death-ligand 1 antibody (αPD-L1)-based immunotherapy. Within the acidic tumor microenvironment (TME), CZP NPs spontaneously release copper and zinc ions and hydrogen peroxide, generating highly oxidative hydroxyl radicals and downregulating iron-sulfur cluster proteins. These actions lead to the disruption of mitochondrial integrity, the release of mitochondrial DNA (mtDNA) and irreversible cuproptosis. The further synergy between mtDNA and zinc ions potentiates the activation of the cGAS-STING signaling pathway, triggering a robust antitumor immune response and sensitizing TNBC to αPD-L1 therapy. Additionally, using an 808 nm near-infrared laser for photothermal therapy significantly augments these effects, resulting in a cascade amplification of therapeutic efficacy against TNBC. The strategic combination of CZP NPs with αPD-L1 markedly bolsters antitumor immunity and suppresses tumor growth. Collectively, our findings present a promising synergistic strategy for TNBC treatment by linking cuproptosis, cGAS-STING activation, photothermal therapy, and immunotherapy.

[†]Bangyi Zhou, Mengyao Chen and Zhixing Hao contributed equally to this work.

*Correspondence:
Jian Huang
drhuangjian@zju.edu.cn
Zhangsen Yu
yzs@usx.edu.cn
Fuming Qiu
qiufuming@zju.edu.cn
Full list of author information is available at the end of the article

Graphical abstract

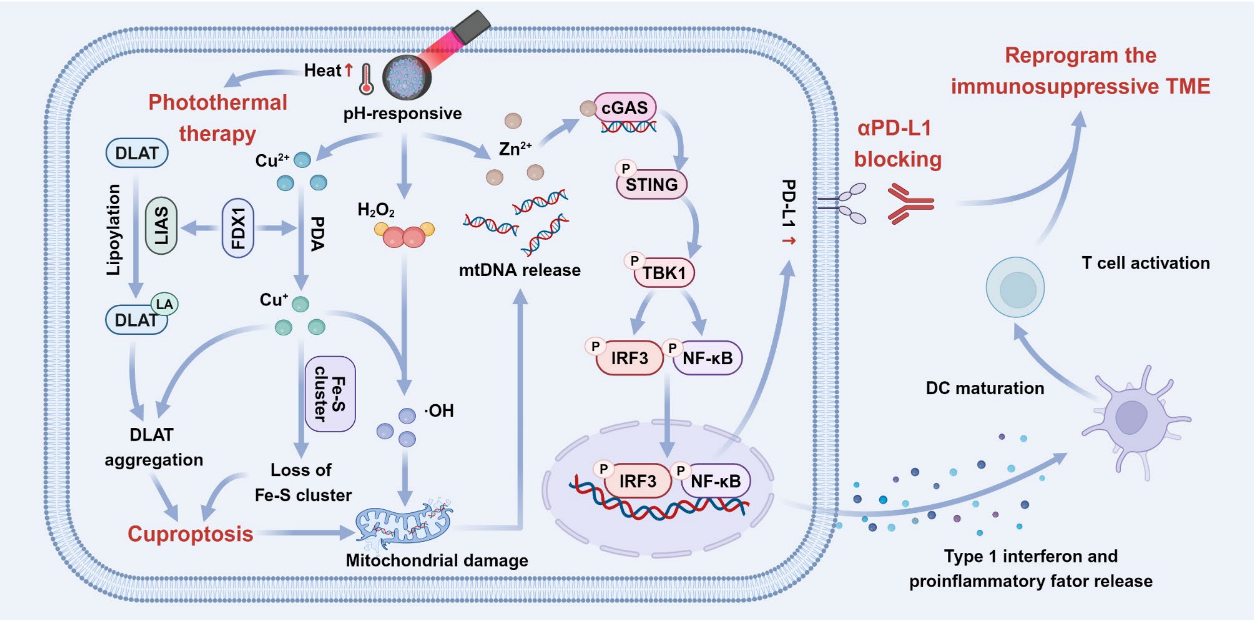

Keywords Triple-negative breast cancer, Immunotherapy, Cuproptosis, cGAS-STING signaling pathway, Photothermal therapy

Introduction

Breast cancer stands as one of the most common malignancies globally, with a rising incidence and a persistently high mortality rate, resulting in considerable economic and social burdens [1]. Defined by the lack of expression of estrogen receptors, progesterone receptors, and human epidermal growth factor receptor 2 (HER-2), triple-negative breast cancer (TNBC), which constitutes approximately 15–20% of all breast cancers [2], exhibiting highly malignant, poor prognosis, higher recurrence rate and lacks effective therapeutic targets [3, 4]. Therefore, there is an urgent need to explore innovative and potent therapeutic strategies for TNBC. In recent years, significant advancements have been made in cancer immunotherapy. Immune checkpoint inhibitors (ICIs), such as αPD-L1 and αPD-1, have demonstrated the ability to activate the host's immune system to target and destroy tumor tissue [5–7]. However, despite the significant clinical efficacy of ICIs in several tumors such as melanoma and lung cancer [8, 9], many TNBC patients still exhibit limited or no response to ICIs. This limitation may be attributed to the immunosuppressive tumor microenvironment (TME) and the relatively low PD-L1 expression rate in TNBC [10–12], which is estimated at around 20% [13], thereby hindering the ability of ICIs to bolster antitumor immunity. A phase III clinical trial for advanced TNBC patients treated with a combination of atezolizumab and paclitaxel did not improve overall survival [14]. Therefore, enhancing the responsiveness and efficacy of immunotherapy in TNBC patients is a vital issue that needs to be solved urgently.

Copper, one of the essential elements that engage in mitochondrial respiration and biosynthesis, plays a crucial role in the normal physiological functioning of cells [15–18]. Hence, copper homeostasis abnormalities can lead to physiological dysfunction, whether caused by a copper deficiency or excess [19]. Cuproptosis, a recently characterized form of cell death, is marked by an excessive accumulation of copper ions within the cell. The intracellular Cu^{2+} can be converted to Cu^+ by ferredoxin 1 (FDX1), which subsequently engages with dihydrolipoamide S-acetyltransferase (DLAT). This interaction triggers protein oligomerization and the loss of iron-sulfur (Fe-S) cluster proteins, disrupting the tricarboxylic acid (TCA) cycle and initiating proteotoxic stress, ultimately leading to cuproptosis [20]. Additionally, due to its Fenton-like activity, Cu^+ facilitates the transformation of hydrogen peroxide (H_2O_2) into highly toxic hydroxyl radicals (·OH), causing oxidative stress [21–23]. Combining cuproptosis and oxidative stress will further induce mitochondrial dysfunction and damage, causing the release of mitochondrial DNA (mtDNA) [24, 25]. Furthermore, emerging evidence indicates that cuproptosis could also induces immunogenic cell death (ICD)

[26], a process capable of reversing the immunosuppressive TME and substantially boosting the effectiveness of ICI-based immunotherapy [27, 28]. Given these effects, cuproptosis presents a promising therapeutic strategy for TNBC. However, the efficacy of cuproptosis is closely linked to the levels of intracellular copper ions, and their accumulation in normal tissues may provoke unnecessary toxicity. Therefore, the precise release of copper ions within the TME is of paramount importance. Moreover, copper-mediated therapies alone are often insufficient for the long-term suppression of tumor growth [29], highlighting the need to combine cuproptosis with other antitumor modalities, such as photothermal therapy (PTT) and immunotherapy.

The activation of the cyclic GMP-AMP synthase (cGAS)-stimulator of interferon genes (STING) signaling pathway in tumor tissue has emerged as a promising approach for improving the effect of immunotherapy [30–32]. Acting as a cytosolic DNA sensor, cGAS detects double-stranded DNA (dsDNA) and triggers the synthesis of cyclic GMP-AMP (cGAMP) [33]. The further binding of cGAMP with STING can activate the TANK binding kinase 1 (TBK1)/interferon regulatory factor 3 (IRF3) axis, which in turn stimulate the expression of type I interferons and pro-inflammatory cytokines, thereby activating dendritic cells (DCs) and initiating an antitumor immune response [34–36]. The mtDNA released from mitochondria damaged by cuproptosis can also activate the cGAS-STING signaling pathway [37, 38], promoting DC maturation and effectively presenting tumor antigens released during cuproptosis to T cells. Consequently, the induction of cuproptosis coupled with the activation of cGAS-STING pathway is expected to synergize in triggering a potent antitumor immune response. Moreover, the transduction of the cGAS-STING pathway can also promotes nuclear factor-κB (NF-κB) activation [39], which in turn upregulates PD-L1 expression on tumor cells [40–42]. Previous studies have confirmed that elevating PD-L1 levels in TNBC can transform ICI-unresponsive tumors into immunogenic ones that are highly sensitive to ICIs [43]. Strikingly, STING pathway activation can also achieve such similar ICI-sensitizing effect through PD-L1 upregulation [44]. Among various cGAS-STING agonists, zinc ions have been identified as crucial modulators of cGAS-STING signal transduction, which can promote the enzymatic catalytic activity of cGAS proteins by facilitating their phase separation [45]. Thus, the strategic integration of copper and zinc ions, in conjunction with ICIs such as αPD-L1, is anticipated to synergistically improve the immunosuppressive TME in TNBC and enhance the efficacy of immunotherapy.

Nevertheless, there are still rare reports focused on cancer therapeutic strategies that integrate cuproptosis with activation of the cGAS-STING pathway to synergistically improve the responsiveness and efficacy of ICIs in TNBC. Herein, we engineered polydopamine (PDA)-coated zinc-copper bimetallic nanoplatforms (Cu-ZnO_2@PDA nanoplatforms, abbreviated CZP NPs), wherein copper ion-loaded zinc peroxide served as the core and PDA formed the shell. CZP NPs maintain their integrity at physiological pH but disintegrate in the acidic TME, selectively releasing zinc and copper ions and H_2O_2. Intracellular Cu^+ enhances the generation of ·OH and induces cuproptosis, leading to mitochondrial damage in tumor cells and the release of substantial mtDNA, activating the cGAS-STING pathway and upregulate the expression of PD-L1 on tumor cells. Moreover, zinc ions further boost the catalytic activity of cGAS and synergistically promote the secretion of type I interferons and inflammatory cytokines, triggering potent innate and adaptive immune responses. Additionally, the PDA coating endows CZP NPs with excellent photothermal conversion capabilities, making them suitable for efficient tumor PTT. Meanwhile, the abundant catechol in PDA serves as a redox mediator, facilitating the regeneration of Cu^+ to amplify the effects of cuproptosis and cGAS-STING activation. Combining CZP NPs with αPD-L1 significantly reshapes the immunosuppressive TME and inhibits tumor growth. Collectively, CZP NPs offer a potent synergistic strategy, demonstrating durable and remarkable efficacy in enhancing antitumor immunotherapy in TNBC (Scheme 1).

Results and discussion

Synthesis and characterization of CZP NPs

The detailed preparation process of the Cu-ZnO_2@PDA nanoplatform (CZP NPs) is summarized in Fig. 2a. Initially, the Zinc acetate dihydrate ($Zn\ (CH_3COO)_2{\cdot}2H_2O$), polyvinylpyrrolidone (PVP), and hydrogen peroxide (H_2O_2) were mixed and stirred at room temperature for 24 h to obtain the ZnO_2 nanoparticles. The presence of PVP could complex zinc ions and assemble them into uniformly spherical nanoparticles. Then, the obtained opalescent solution was stirred with cupric chloride dihydrate ($CuCl_2{\cdot}2H_2O$) for 4 h, forming Cu-ZnO_2 (CZ) nanoparticles. Adding copper ions altered the solution's color to a soft green. Ultimately, through the in situ self-polymerization of dopamine, the nanoparticles were coated with polydopamine (PDA), and a brownish-black solution was obtained (Fig. 2b). Transmission electron microscope (TEM) images revealed that a pronounced core-shell structure was constructed after the PDA coating on the surface of Cu-ZnO_2 (Fig. 2c). Meanwhile, the energy dispersive X-ray (EDS) mapping illustrated that the nanoparticles consisted of carbon (C), nitrogen (N), oxygen (O), copper (Cu), and zinc (Zn) elements, validating the successful synthesis of CZP NPs (Fig. 2d). To

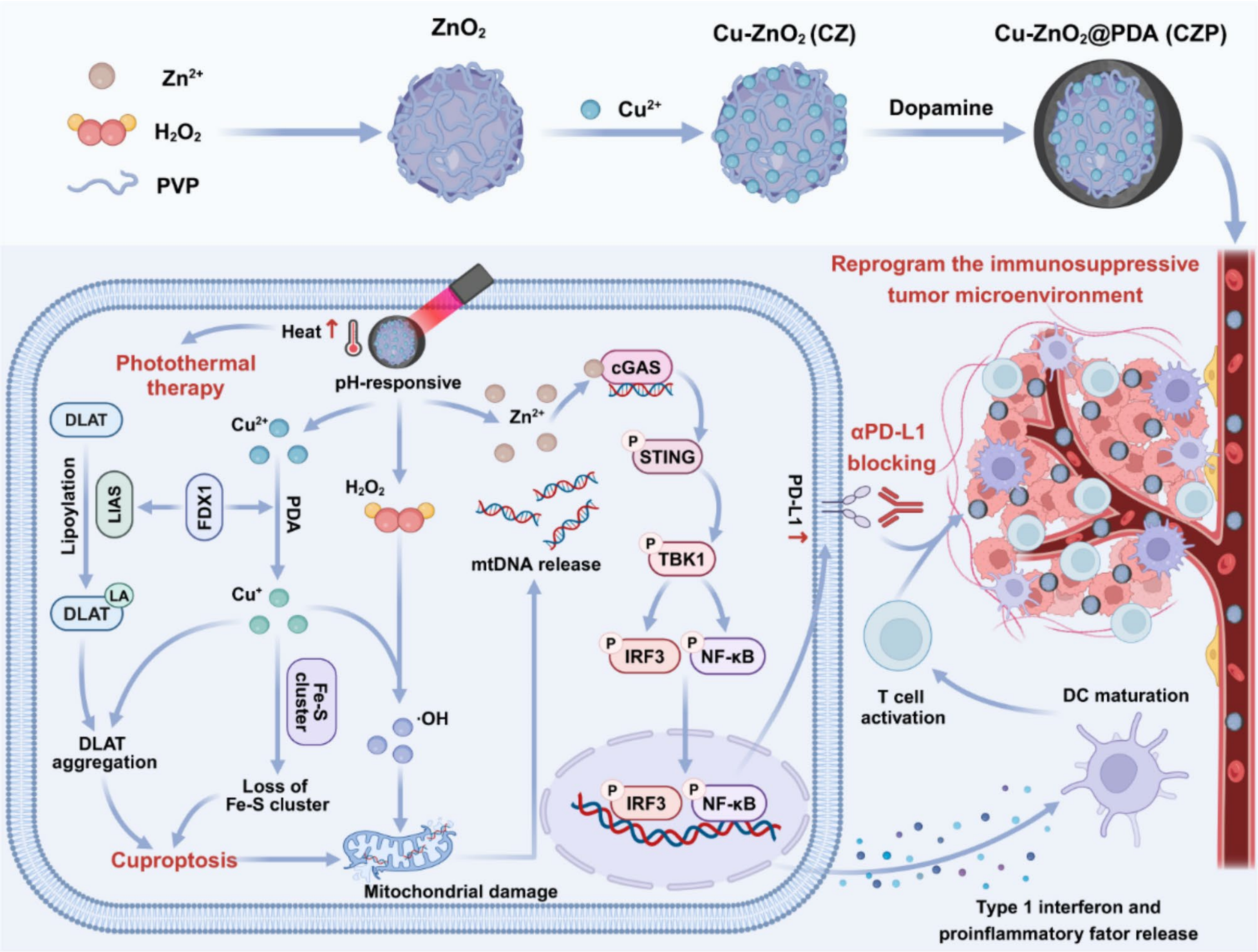

Fig. 1 Schematic diagram of the Cu-ZnO_2@PDA nanoplatforms combined with αPD-L1 for enhancing TNBC immunotherapy

further verify the composition of CZP NPs especially the valence state of elements, we conducted X-ray photoelectron spectroscopy (XPS) analysis with a total spectrum confirmed the simultaneous presence of Cu, Zn, C, N, and O elements in CZP NPs (Fig. S1a). Specifically, Figure S1b displays two distinct peaks at 1045.1 and 1022.0 eV, corresponding to the Zn 2p1/2 and Zn 2p3/2 orbitals of Zn^{2+}, respectively. Furthermore, Figure S1c indicates that copper ions exist in both Cu^{2+} (934.7 eV) and Cu^{+} (932.9 eV) valence states, with a ratio of 1.24. Dynamic light scattering (DLS) measurement disclosed that the hydrodynamic diameter of CZP NPs is approximately 177.2 nm, notably exceeding that of ZnO_2 (~121.8 nm) and CZ (~ 120.1 nm), accompanied by the polydispersity index (PDI) were measured to be 0.07, 0.12, 0.09, respectively (Fig. 2e and f). Furthermore, the zeta potential of ZnO_2 and CZ nanoparticles showed a positive charge of 37.0 ± 0.42 mV and 29.7 ± 0.78 mV, respectively, and eventually regulated at -21.2 ± 1.13 mV after PDA adhesion (Fig. 2g). The results of Fourier transform infrared spectroscopy (FT-IR) showed an absorption band at approximately 1510 cm^{-1} corresponding to the shear vibration of N – H (Fig. 2h), confirming the successful coating of PDA. Notably, within the spectral range of 250 to 1000 nm, the CZP NPs exhibited markedly higher absorption values than those of ZnO_2 and CZ, suggesting their promising photothermal properties (Fig. 2i).

Photothermal performance evaluation

Figure 2i shows that CZP NPs possess a broad absorbance across the wavelength range of 250–1000 nm. Notably, at an equivalent concentration, the absorbance of CZP NPs at 808 nm is 9.5 times that of ZnO_2 and 4.3 times that of CZ, highlighting their excellent photothermal therapeutic potential. Therefore, we next evaluated the photothermal performance of CZP NPs. Following a 5-minute exposure to an 808 nm laser irradiation, CZP NPs showed a pronounced temperature elevation correlated with increasing irradiation power density and concentration. The CZP NPs at the concentration of 500 μg/mL exhibited a significant temperature increase (ΔT) of 24.63 °C (3 W/cm^2), markedly surpassing the H_2O, ZnO_2,

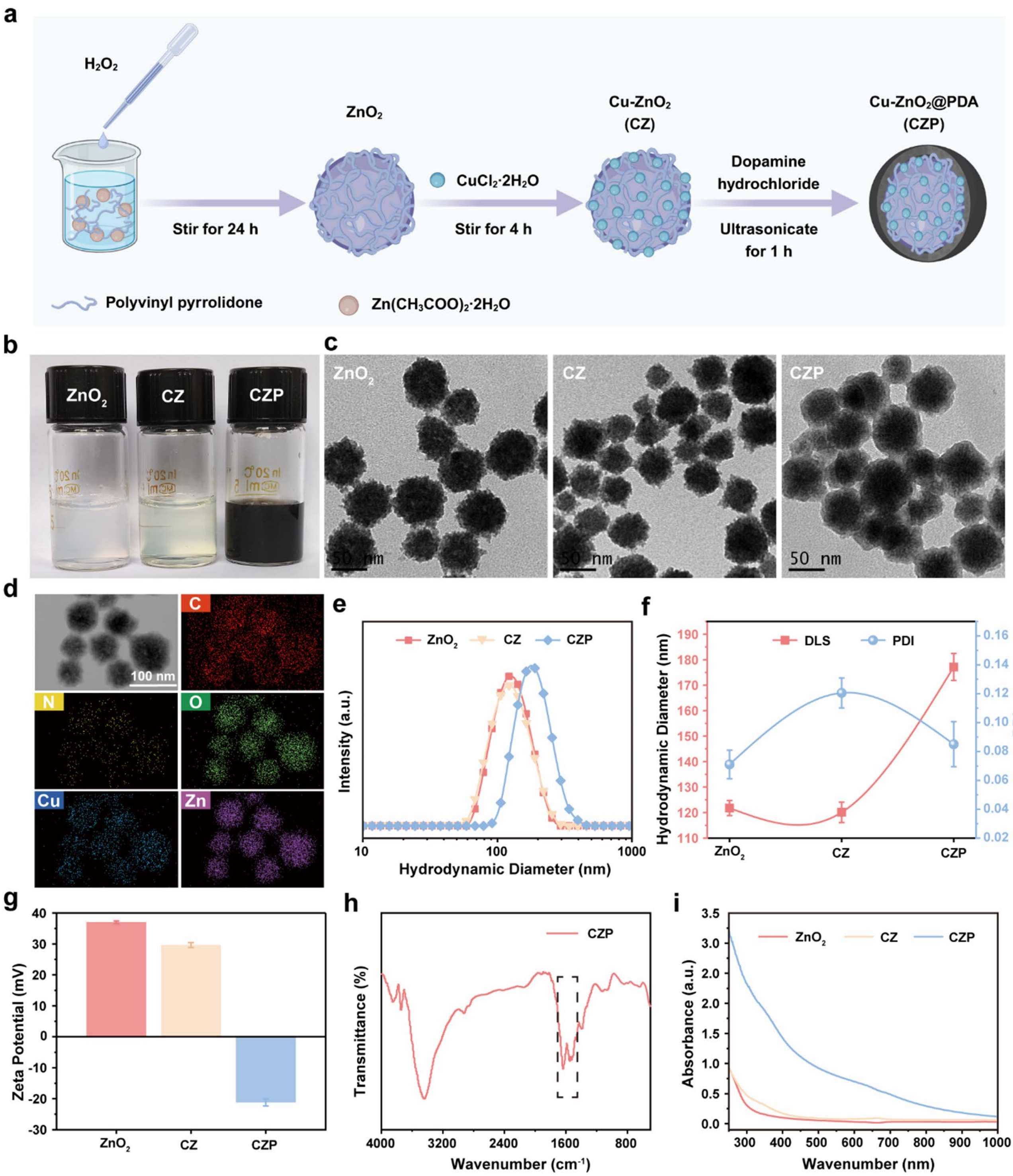

Fig. 2 Synthesis and characterization of CZP NPs. **(a)** Schematic illustration of the synthesis of CZP NPs. **(b)** Photograph and **(c)** TEM micrograph of ZnO_2, CZ, and CZP NPs. **(d)** The EDS mapping of C, N, O, Cu, and Zn of prepared CZP NPs. **(e, f)** The hydrodynamic diameter, polydispersity index, and **(g)** zeta potentials of ZnO_2, CZ, and CZP NPs. **(h)** FT-IR spectrum of CZP NPs. **(i)** UV-Vis spectra of ZnO_2, CZ, and CZP NPs

and CZ groups, which were only 1.90 °C, 1.33 °C, and 1.84 °C, respectively (Fig. 3a, b and Fig. S2). This temperature rise is adequate to induce necrosis and apoptosis in tumor cells. The changes shown in the thermal images were also consistent with the above results (Fig. 3c). Subsequently, the photothermal conversion efficiency (η) of CZP NPs was further assessed. After 20 min of 808 nm NIR irradiation at 3 W/cm², the temperature of CZP NPs

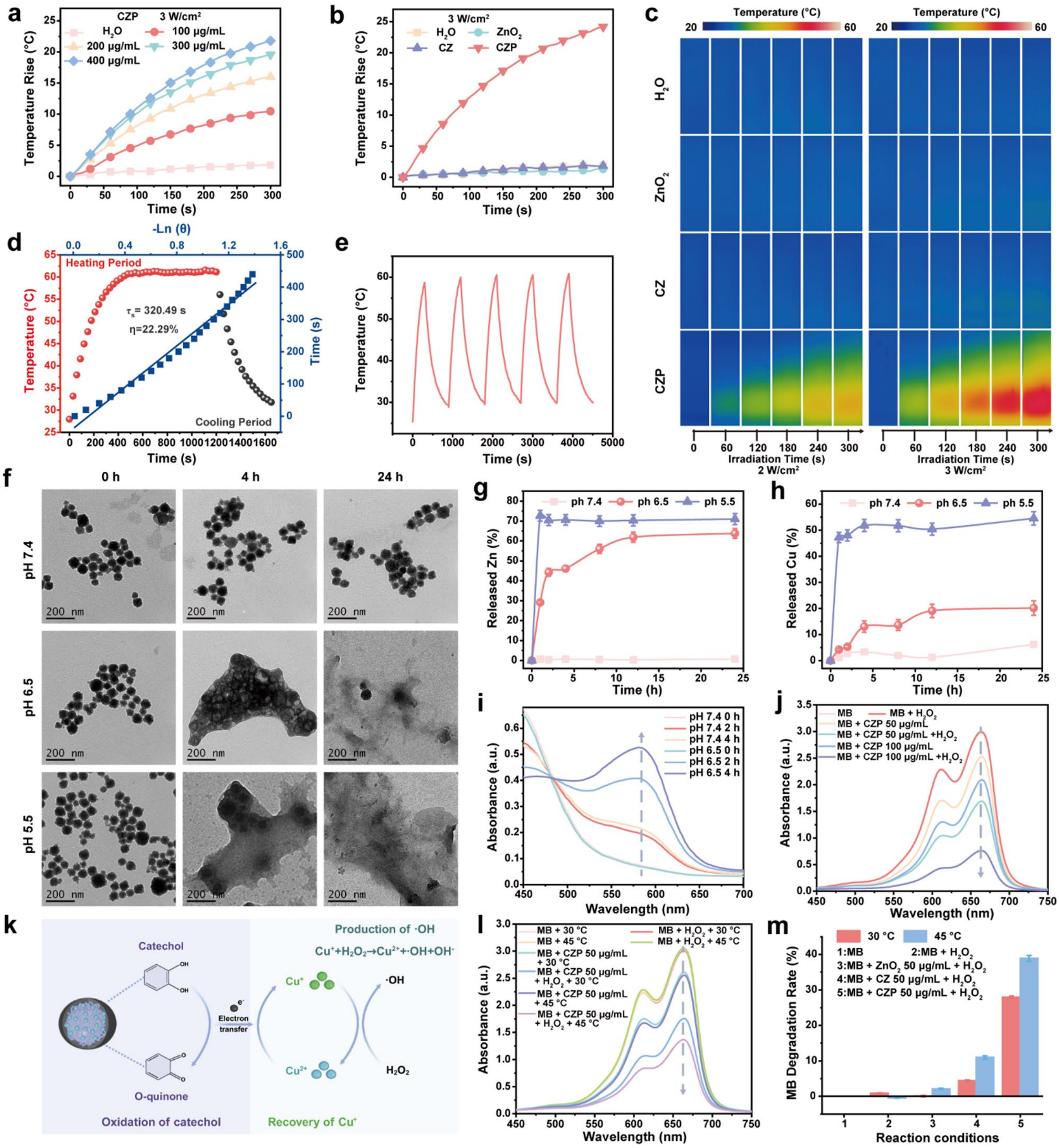

Fig. 3 Photothermal, pH-responsive degradation, and ROS generation capabilities of CZP NPs. **(a)** Concentration-dependent temperature-time curves of CZP solutions. **(b)** Temperature-time curves and **(c)** thermal images (500 μg/mL) of H_2O, ZnO_2, CZ, and CZP solutions under NIR irradiation. **(d)** Photothermal conversion efficiency and **(e)** recycling-heating curves of CZP solution under NIR irradiation (3.0 W cm^2). **(f)** TEM images of CZP NPs following incubation at various pH levels. **(g)** The release of zinc and **(h)** copper ions from CZP NPs at different pH conditions. **(i)** UV–Vis spectra of the CZP NPs incubated with a Hydrogen Peroxide Assay Kit at pH 7.4 or 6.5 conditions. **(j)** UV–Vis spectra of MB after incubated with different concentrations of CZP NPs. **(k)** The mechanism of the electron transfer of CZP NPs for promoting the Fenton-like reaction. **(l)** UV–Vis spectra of MB and **(m)** MB degradation rates across various groups

at 500 μg/mL reached 61.14℃, whereas the temperature of H_2O merely reached 30.78℃. The η value of CZP NPs was then calculated to be 22.29% (Fig. 3d and Fig. S3), which is not significantly different from the published result of PDA nanoparticles [46]. The photothermal performance exhibited by CZP NPs fully demonstrates that the Cu-ZnO_2 core does not considerably impair the photothermal performance of PDA. Moreover, after five consecutive heating-cooling cycles, there were no significant changes in the real-time temperature change curve and UV-Vis spectra of the CZP solution before and after laser irradiation, demonstrating its excellent photothermal stability (Fig. 3e and Fig. S4). Consequently, the CZP NPs we have developed exhibit excellent photothermal capabilities and can be applied to subsequent tumor photothermal therapy.

pH-triggered Zn-Cu ions/H_2O_2 release and ROS generation

According to our hypothesis, CZP NPs can selectively decompose and release zinc, copper ions, and H_2O_2 within the acidic TME. To assess the pH-responsive behavior of CZP NPs, TEM was utilized to observe their morphological changes after undergoing different pH conditions (pH = 7.4, 6.5, and 5.5). As anticipated, the CZP NPs were almost wholly decomposed within 24 h at pH 5.5 while remaining stable at pH 7.4 (Fig. 3f). Subsequently, an inductively coupled plasma-atomic emission spectrometer (ICP-AES) was utilized to investigate the pH-dependent release of zinc and copper ions. The results showed that the release of zinc and copper ions in a pH 7.4 buffer solution was conspicuously sluggish, with merely 0.7% and 6.2%, respectively, over a 24-hour incubation (Fig. 3g and h). In stark contrast, the release rates at pH 5.5 increased to 71% and 54.5%, respectively. Furthermore, to investigate the impact of PDA coating on the degradation of CZP NPs, a comparative analysis between CZ and CZP was conducted. Despite a slight reduction in the release rate observed after the PDA coating, CZP NPs could rapidly decompose and release a substantial amount of metal ions within 24 h for tumor treatment (Fig. S5). In addition, we also analyzed the release of H_2O_2 from CZP NPs by using a hydrogen peroxide assay kit. The detection reagent can recognize H_2O_2 and react to form a purple compound, exhibiting a maximum absorption peak of around 560 nm. Co-incubation of CZP NPs with the detection reagent at pH 6.5 significantly enhanced the absorbance of the solution at 560–580 nm (Fig. 3i), demonstrating CZP's capacity to release H_2O_2 under acidic conditions.

Theoretically, the Cu^+ and H_2O_2 in the TME could induce the generation of ·OH and Cu^{2+}*via* the Fenton-like catalytic reaction [47–49], thereby promoting oxidative stress within tumor cells. Methylene blue (MB) was chosen as the indicator to assess the capacity of ·OH generation, which is a dye probe that ·OH can cause MB to fade. As shown in Fig. 3j, upon co-incubation of CZP NPs with H_2O_2 and MB, the color of the solution progressively lightened from light blue as the CZP concentration increased. Simultaneously, the absorption peak of MB in the range of 600–700 nm gradually decreased. However, MB co-incubated with H_2O_2 alone showed no significant color or absorption spectra changes. Furthermore, we compared the ·OH generation capabilities among different nanoparticles. In the presence of H_2O_2, MB was degraded by 100μg/mL CZP NPs, with a degradation rate of 44.2%, approximately 4.25 times higher than that of the CZ group (Fig. S6a-c). However, the proportion of copper ions in CZ, as previously determined by ICP analysis, was approximately 11.58%, surpassing the 8.93% found in CZP NPs (Fig. S7). The superior Fenton-like reaction performance of CZP NPs may be attributed to the presence of PDA. The abundant catechol in PDA can act as a redox mediator [50], facilitating the transfer of electrons to Cu^{2+} and promoting the regeneration of Cu^+. This process helps maintain high catalytic activity in the Fenton-like reaction and continuously generates ·OH (Fig. 3k). Finally, we examined the influence of temperature on the catalytic efficiency of CZP NPs. These nanoparticles exhibited enhanced catalytic activity at 45 °C, achieving an MB degradation rate of 38.9% at a concentration of 50 μg/mL, which was considerably higher than the 27.9% observed at 30 °C (Fig. 3l, m and Fig. S6d, e). Therefore, the experimental results confirmed that CZP NPs can spontaneously release zinc and copper ions, H_2O_2, and generate ·OH in the acidic TME.

In vitro cellular uptake and cytotoxicity

Driven by the significant photothermal and Fenton-like catalytic activities of CZP NPs, we hypothesize that these nanoparticles can efficiently kill tumor cells in vitro. To monitor the cellular uptake behavior of CZP NPs, FITC labeled CZP to obtain FITC-CZP. Concurrently, we labeled the cell membrane and nucleus to visualize the intracellular localization and distribution of CZP. The confocal laser scanning microscope (CLSM) results revealed that distinct green fluorescence was observed following a 4-hour co-incubation of FITC-CZP with 4T1 cells (Fig. 4a). The fluorescence was predominantly colocalized with the cytoplasm, indicating successful internalization of CZP into the cells. The flow cytometry was utilized for further analysis. As shown in Fig. 4b-e, a gradual increase in the fluorescence intensity in 4T1 cells was detected with increasing CZP concentration and prolonged incubation time. After 8 h of incubation with 40 μg/mL FITC-CZP, the mean fluorescence intensity (MFI) in 4T1 cells was approximately 1.7-fold that of the 4-hour incubation and about 3.0-fold that of the 1-hour

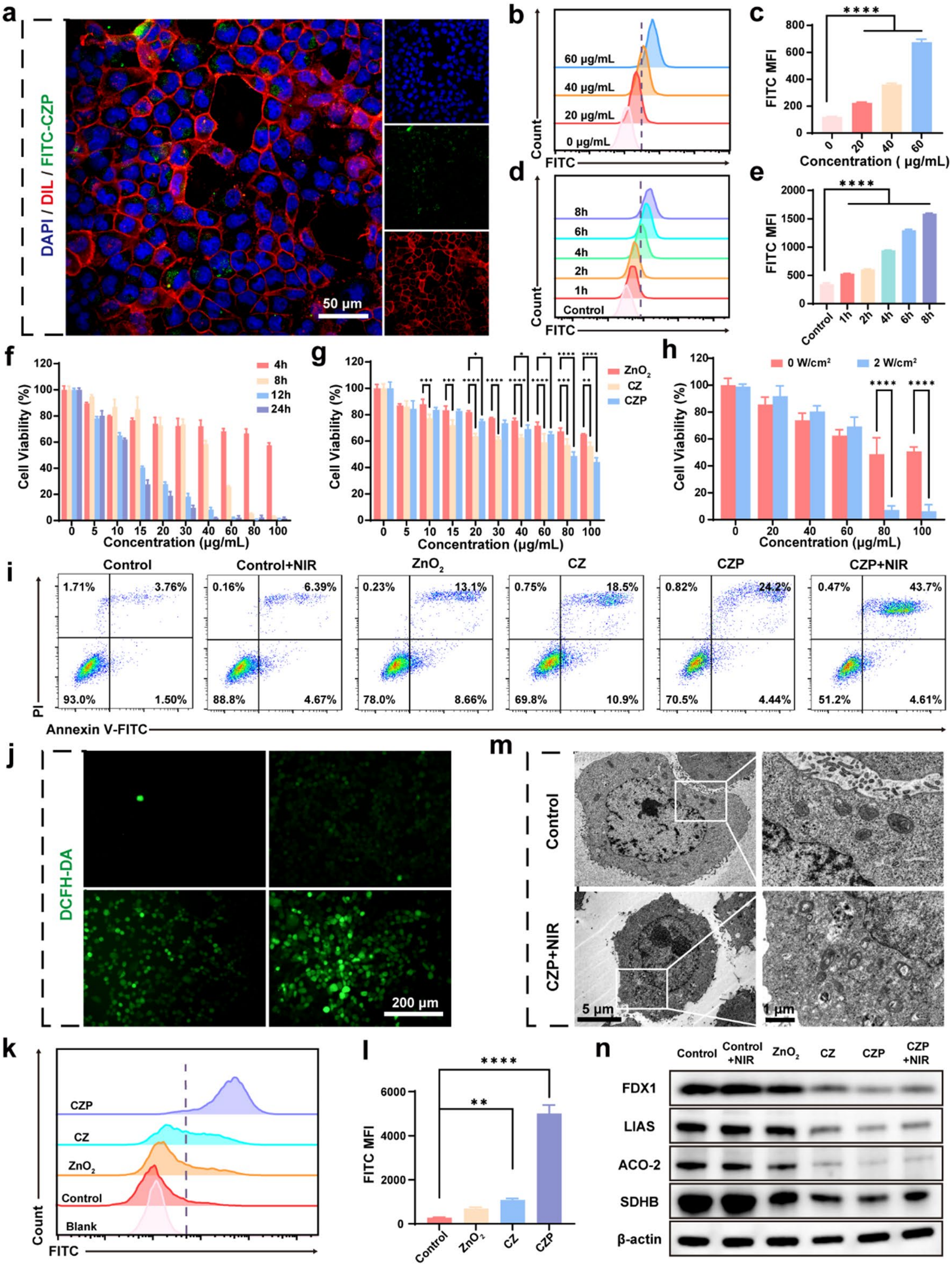

Fig. 4 In vitro cellular uptake and antitumor effect of CZP NPs. **(a)** Representative confocal microscopy images of 4T1 cells following a 4-hour incubation with FITC-CZP NPs. The cell nuclei were stained with DAPI (blue) and the cell membranes with Dil (red). **(b-e)** Flow cytometric profiles and corresponding quantification of 4T1 cells incubated with FITC-CZP NPs over various concentrations and time points (*n* = 3). **(f-h)** The cell viability of 4T1 cells after various treatments (*n* = 3). **(i)** Flow cytometric assessment of apoptosis and necrosis in 4T1 cells. **(j-l)** Fluorescent imaging and flow cytometric analysis of intracellular ROS levels of 4T1 cells. **(m)** Bio-TEM images of untreated 4T1 cells or treated with CZP + NIR. **(n)** Western blot analysis of FDX1, LIAS, ACO-2, and SDHB from 4T1 cells following various treatments

incubation. These findings demonstrate that CZP NPs could rapidly be taken up by 4T1 cells.

The cytotoxicity of various treatments was assessed using the Cell Counting Kit-8. As shown in Fig. 4f, CZP NPs exhibited an evident dose and time-dependent cytotoxicity against 4T1 cells, with cell-killing rates reaching approximately 91.7% and 98.1% at a concentration of only 40 μg/mL after 12 and 24 h of incubation, respectively. We further analyzed the differences in cytotoxicity among the ZnO_2, CZ, and CZP NPs. After 4 h of co-incubation with 4T1 cells, ZnO_2 and CZ displayed limited cytotoxicity, even at a high concentration of 100 μg/mL, with cell-killing rates of merely 34.7% and 43.8%, respectively. In contrast, CZP NPs achieved a cell-killing rate of around 56.0% (Fig. 4g). Moreover, when exposed to an 808 nm laser at a power density of 2 W/cm^2 for 5 min, the killing rate of CZP NPs further increased to an impressive 93.8% (Fig. 4h). Subsequently, we investigated the apoptosis and necrosis rates in 4T1 cells following various treatments using the Annexin V-FITC Apoptosis Detection Kit. Flow cytometry analysis revealed that the apoptotic and necrotic rate of 4T1 cells treated with CZP + NIR was 47.7%, which was 8.4, 7.7, and 1.7 times higher than that of Control, Control + NIR, and CZP treatment groups, respectively (Fig. 4i and Fig. S8). These results confirm that the combination strategy of CZP + NIR could elicit satisfactory synergistic antineoplastic effects in vitro.

In vitro cuproptosis induced by CZP NPs

The substantial accumulation of copper ions within tumor cells induces intracellular oxidative stress by generating toxic ·OH and promotes the aggregation of lipoylated proteins and the loss of Fe-S cluster proteins, which leads to the disruption of the tricarboxylic acid (TCA) cycle in mitochondrial metabolism and induces cuproptosis [51]. Previous experiments have confirmed that CZP NPs can release many copper ions in an acidic environment. Therefore, we further investigated the impact of released copper ions on tumor cells. Firstly, the Reactive Oxygen Species Assay Kit (DCFH-DA) was utilized to evaluate the intracellular reactive oxygen species (ROS) levels. Images obtained from the inverted fluorescence microscope distinctly highlighted differences in fluorescence intensity across various treatment groups (Fig. 4j). 4T1 cells treated with CZP NPs exhibited the most robust green fluorescence, suggesting the highest production of ROS. Flow cytometry results showed that the MFI of CZP-treated cells was 18.2, 7.2, and 4.6 times greater than that of the Control, ZnO_2, and CZ groups, respectively (Fig. 4k and l). Because excessive ROS generation can induce mitochondrial damage and subsequent release of mtDNA [52], we conducted a Bio-TEM to analyze the changes in mitochondria structure in 4T1 cells following CZP treatment. The images revealed that CZP treatment induced significant mitochondrial damage in 4T1 cells compared to the control group, characterized by mitochondrial swelling, shortened cristae, and the formation of vacuoles (Fig. 4m).

Furthermore, we examined the expression levels of Fe-S cluster proteins in 4T1 cells using Western blot analysis. As depicted in Fig. 4n, tumor cells treated with ZnO_2 showed no significant change in the expression of Fe-S cluster proteins compared to the Control group, which is consistent with our expectations. Notably, CZP and CZP + NIR treatments significantly downregulated the expression of Fe-S cluster proteins, including FDX1, LIAS, ACO-2, and SDHB. These findings confirm the bimetallic nanoplatform successfully induced the 4T1 cells' cuproptosis. Collectively, CZP NPs have the potential to elevate intracellular ROS levels, cause mitochondrial damage, and induce cuproptosis.

mtDNA release and cGAS-STING pathway stimulation

To ascertain whether mitochondrial damage induced by CZP NPs could trigger the release of mtDNA, we employed Quantitative real-time PCR (qPCR) assays to measure the release of mtDNA into the cytoplasm. As shown in Fig. 5a, treatments with ZnO_2, CZ, and CZP NPs induced the release of mtDNA in 4T1 cells, with the CZP + NIR therapy resulting in the highest levels of detected mitochondrial DNA. Specifically, mtDNA levels were 3.49-fold higher than the Control, 3.19-fold higher than the Control + NIR, 2.10-fold higher than the ZnO_2, 1.52-fold higher than the CZ, and 1.37-fold higher than the CZP alone. Previous research has indicated that mtDNA released from damaged mitochondria can also mediate the activation of the cGAS-STING signaling pathway [37, 38]. Additionally, zinc ions are crucial in modulating cGAS activity within cells. They promote cGAS activation by facilitating its phase separation, activating STING protein, and initiating downstream signaling pathways. To verify the activation of the cGAS-STING signaling pathway after mtDNA release induced by various treatments, we analyzed the expression levels of *cGAS* and related genes *via* qPCR. The findings indicated that treatments with laser irradiation alone, ZnO_2, and CZ had limited effects on *cGAS* expression, approximately 0.96, 1.57, and 2.28 times that of the control group, respectively. In contrast, combining CZP with NIR irradiation yielded the most significant upregulation of *cGAS* expression, approximately 7.84 times higher than the control. (Fig. 5b). This disparity may be attributed to the differential of mtDNA release.

Further analysis revealed that the CZP + NIR treatment also significantly enhanced the expression of cGAS target genes, including *IFNB1*, *CXCL10*, *IGS56*, and *ISG15* (Fig. 5c-f), confirming the effective activation of the

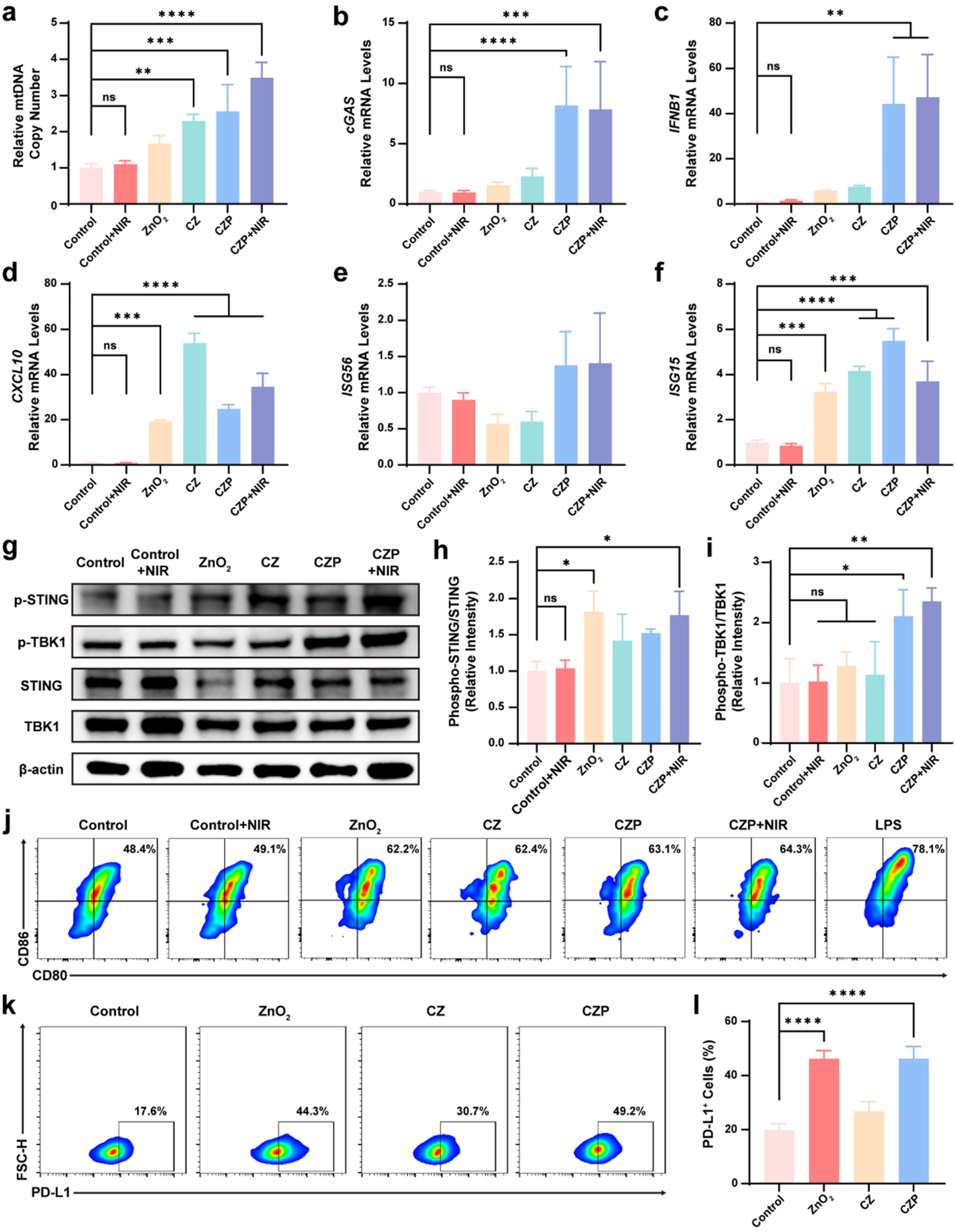

Fig. 5 CZP NPs promote the activation of the cGAS-STING signaling pathway. **(a)** The detection of mitochondrial DNA copy number in 4T1 cells after indicated treatments ($n = 4$). **(b)** The expression of *cGAS* and *cGAS* target genes including **(c)***IFNB1*, **(d)***CXLC10*, **(e)***ISG56*, and **(f)***ISG15* in 4T1 cells with the indicated treatment ($n = 3$–5). **(g-i)** Western blot analysis of p-STING, p-TBK1, STING, and TBK1 protein levels in 4T1 cells after various treatment. *β*-actin was used as the control ($n = 3$). **(j)** Representative flow cytometry images of mature DCs after different treatments. **(k)** Representative flow cytometry images and **(l)** corresponding quantification data of PD-L1 expression on 4T1 cells following different treatments ($n = 3$)

cGAS-STING pathway. Notably, the expression levels of *IFNB1* and *CXCL10* in 4T1 cells after CZP + NIR treatment were substantially increased, reaching 47.17-fold and 34.57-fold that of the control group, respectively. Moreover, Western blot analysis of STING and TBK1 protein phosphorylation levels demonstrated that the CZP + NIR treatment increased the phosphorylation of STING and TBK1 compared to other groups. The ratio of phosphorylated STING to total STING was approximately 1.77-fold that of the control group, while the ratio of phosphorylated TBK1 to total TBK1 was 2.25-fold (Fig. 5g-i). These findings confirm that the cytosolic release of mtDNA triggered by CZP + NIR treatment, in combination with zinc ions, can effectively activate the cGAS-STING signaling pathway.

Given that the activation of the cGAS-STING pathway can enhance the maturation and activation of antigen-presenting cells (APCs) by promoting the secretion of cytokines such as type I interferons and CXCL10, we assessed the impact of CZP NPs on DCs maturation in vitro. Initially, we isolated bone marrow-derived dendritic cells (BMDCs) from BALB/c mice and co-cultured them with the supernatant of 4T1 cells that had undergone various treatments for 24 h. We then evaluated DCs maturation using flow cytometry. As shown in Fig. 5j and S9, compared to the Control group, the Control + NIR treatment did not significantly alter the percentage of mature DCs ($CD11c^{+}CD80^{+}CD86^{+}$), whereas the CZP + NIR treatment significantly increased the average level from approximately 52.1 to 63.9%, aligning our expectations.

Notably, the activation of STING not only stimulates the secretion of type I interferons by activating the TBK1/IRF3 axis but also triggers NF-κB activation, which is intimately linked to PD-L1 expression on tumor cells [40–42]. And the level of PD-L1 expression in TNBC has been confirmed to be closely related to the efficacy of ICIs [43]. Accordingly, we further examined the expression of PD-L1 on tumor cells after exposure to various treatments. Flow cytometry results indicated that the average PD-L1 expression on 4T1 cells treated with CZP NPs was significantly higher than that of the Control group, approximately 2.3 times greater (Fig. 5k and l). This finding was further confirmed by qPCR analysis (Fig. S10). These results suggest that the CZP NPs can upregulate PD-L1 expression in tumor cells, implying that combining CZP NPs with αPD-L1 could be a promising approach for cancer treatment.

Transcription analysis of CZP + NIR treated 4T1 cells

We investigated the transcriptomic changes in 4T1 cells treated with CZP NPs combined with NIR laser irradiation through RNA sequencing. Principal component analysis revealed a distinct separation between the CZP + NIR and Control groups (Fig. 6a). Remarkably, 7548 genes exhibited significant differential expression ($p < 0.05$) following CZP + NIR treatment compared to the Control, with 4770 genes upregulated and 2778 genes downregulated (Fig. 6b). Subsequent analysis showed substantial downregulation of gene expression related to Fe-S cluster proteins (*e.g.*, *LIAS*), mitochondrial proteins (*FDXR*, *OMA1*), TCA cycle and respiratory electron transport (*e.g.*, *DBT*, *OGDH*), and DNA repair (*e.g.*, *RAD51*, *MRNIP*) in 4T1 cells following CZP + NIR treatment (Fig. 6c). Conversely, the expression of genes associated with the interferon signaling pathway (*e.g.*, *cGAS*, *IFITT*, *ISG15*, *CXCL10*) and *CD274* (*PD-L1*) was markedly upregulated in the CZP + NIR group, consistent with prior experimental observations. Gene ontology (GO) enrichment analysis highlighted the involvement of biological processes in the CZP + NIR group, such as 'Cellular response to stress', 'Regulation of immune system process', 'Response to oxidative stress', 'Negative regulation of growth', and 'Cellular response to copper ion' (Fig. 6d and Fig. S11). Kyoto Encyclopedia of Genes and Genomes (KEGG) enrichment analysis further demonstrated a significant correlation between multiple pathways and the therapeutic effects mediated by CZP + NIR treatment, including the TNF signaling pathway, FoxO signaling pathway, Toll-like receptor signaling pathway, IL-17 signaling pathway, and Cytokine-cytokine receptor interaction (Fig. 6e and Fig. S12). These findings suggest that CZP + NIR treatment induces cytotoxicity in tumor cells *via* cuproptosis and oxidative stress while enhancing antitumor immune responses by regulating immune-related signaling pathways. Additionally, enrichment of the NF-κB signaling pathway in the CZP + NIR treatment group was also observed (Fig. 6e), which is closely related to the expression of PD-L1 in tumor cells. Moreover, Gene set enrichment analysis (GSEA) confirmed the robust upregulation of pathways involved in the cellular response to oxidative stress, response to heat, and cytokines and inflammatory response following CZP + NIR treatment (Fig. 6f-h), aligning with the above-mentioned finding.

In vivo biosafety and biodistribution evaluation

Ensuring biosafety and biocompatibility is crucial for the safe application of pharmaceuticals in vivo. Therefore, we initially assessed the biosafety of CZP NPs. Healthy ICR mice were administered CZP NPs at escalating doses (10, 20, 30, 40, and 50 mg/kg) *via* tail vein injection, with saline as a control. The mice were monitored for changes in body weight and behavior every other day. After 28 days, each group's blood and major organs were harvested for further analysis. The results showed no discernible behavioral abnormalities of mice were observed, and body weights steadily increased over time

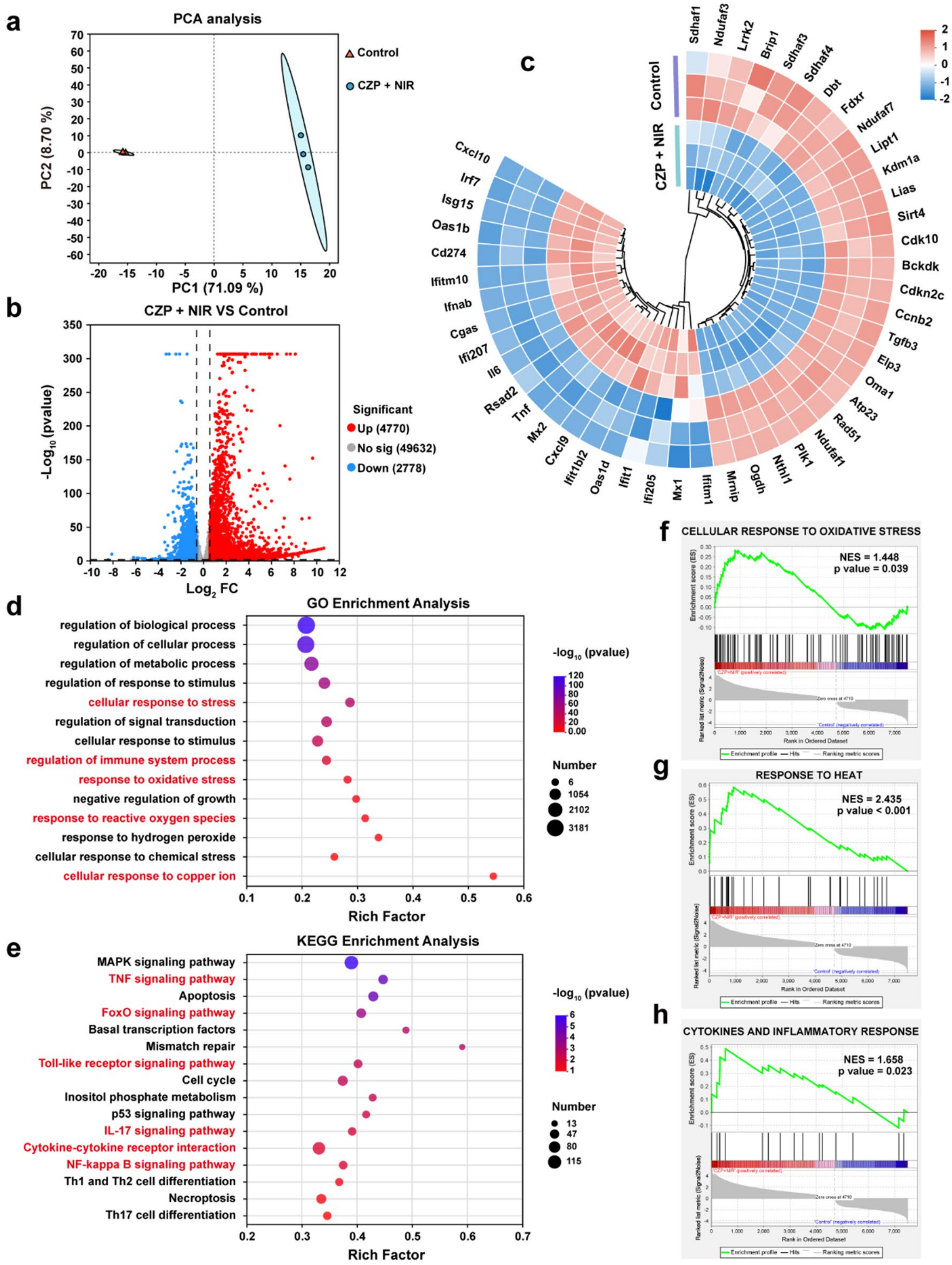

Fig. 6 RNA sequencing analysis of 4T1 cells in control and CZP + NIR treatment groups. **(a)** Principal component analysis, **(b)** volcano plot, and **(c)** heat map of differentially expressed genes in CZP + NIR group compared to Control. **(d)** GO, **(e)** KEGG, and **(f-h)** GSEA enrichment analysis of differentially expressed genes in the CZP + NIR group

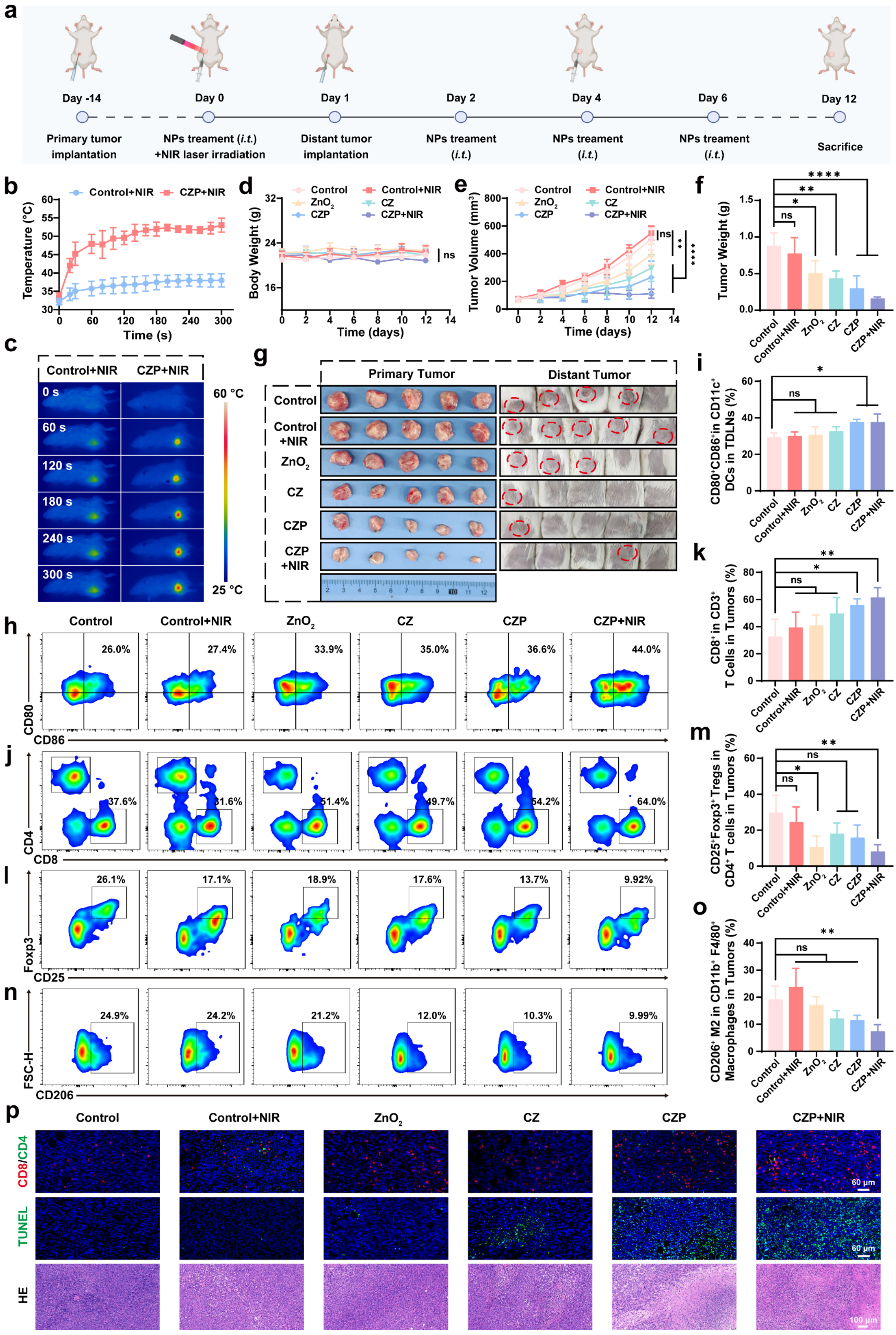

Fig. 7 (See legend on next page.)

(See figure on previous page.)

Fig. 7 CZP mediated therapy on 4T1 tumor. **(a)** Schematic illustration of the experimental schedule for 4T1 tumor-bearing mice. **(b)** Temperature-time curves and **(c)** thermal images of tumor-bearing mice under NIR irradiation (1 W/cm^2, *n* = 5). **(d)** Body weight changes of mice over 12 days. **(e)** Tumor growth curves, **(f)** tumor weights and **(g)** corresponding photographs of primary and distant tumors (*n* = 5). Representative flow cytometry plots and corresponding quantifications of **(h, i)** mature DCs in TDLNs, **(j, k)** CD3$^+$ CD8$^+$ T cells, **(l, m)** Tregs, and **(n, o)** M2 phenotype tumor-associated macrophages in tumors from mice following various treatments (*n* = 4). **(p)** Immunofluorescence staining of CD8$^+$ and CD4$^+$ T cells, TUNEL, and H&E staining of tumor tissues from mice given various treatments

without significant differences between different doses of CZP-treated groups and the saline (Fig. S13), which suggests the CZP NPs exhibit low systemic toxicity even at the maximum tested dose of 50 mg/kg. The organ coefficients and macroscopic examinations of the main organs (heart, liver, spleen, lung, and kidney) also confirmed that CZP treatment did not cause atrophy of the major organs at different doses (Figs. S14 and S15). Subsequently, we scrutinized the physiological and biochemical parameters of the blood in mice in each group. The levels of total protein (TP), blood urea nitrogen (BUN), creatinine (CREA), and routine blood parameters in CZP-treated mice were not significantly different from the saline (Figs. S16 and S17). However, it should be pointed out that CZP treatment moderately reduced the levels of alanine aminotransferase (ALT), aspartate aminotransferase (AST), uric acid (UA), and creatine kinase (CK) in the serum. Even at a high concentration of 50 mg/kg, the serum AST and ALT levels in mice remained low, at only 74.8% and 61% of the control group's levels, respectively. This indicates that CZP NPs have low toxicity to normal tissues and do not cause liver cell damage, suggesting their potential for in vivo applications. Finally, histological examination of the major organs using hematoxylin and eosin (H&E) staining revealed no significant morphological or pathological alterations in mice treated with CZP NPs relative to the saline-treated group (Fig. S18). Collectively, these results demonstrate the outstanding biosafety of CZP NPs in vivo.

Next, we constructed an orthotopic breast cancer model based on 4T1 cells to investigate the biodistribution of CZP NPs in vivo. Indocyanine green (ICG)-labeled CZP NPs (CZP-ICG) were injected *via* tail vein, and the subsequent fluorescence intensity in the mice was monitored at various time intervals using an In Vivo Imaging System (IVIS). The results showed that a strong fluorescence signal was still present at the tumor site even 24 h after the injection (Fig. S19), indicating the accumulation of CZP-ICG within the tumor. Moreover, mice were sacrificed 4- and 24-hours post-injection, and major organs and tumor tissues were harvested for ex vivo bioimaging. The results showed that the total fluorescence intensity in tumors 24 h after administration was approximately 1.4×10^8 p/s, ranking third among all tissues, following the liver and spleen (Fig. S20). This indicates that CZP NPs can rapidly target and accumulate at the tumor site, which is highly beneficial for its application. Additionally, it is noteworthy that CZP can reach the kidneys through the bloodstream, and the fluorescence signals in all organs at 24 h are lower than those at 4 h. This suggests that CZP may be excreted through the kidneys, thereby reducing its accumulation in normal tissues. Furthermore, histological sections of major organs after HE staining confirmed no significant CZP NPs deposition 28 days after *i.t.* injection (Fig. S18), indicating that our synthesized CZP has good biocompatibility and is metabolizable.

In vivo antitumor effect of CZP NPs

The therapeutic effect of CZP NPs was further evaluated in vivo. Initially, a primary orthotopic breast tumor model was established by injecting 4T1 cells into the left fourth mammary fat pad of BALB/c mice. Once tumors reached 60–100 mm^3, mice were randomly divided into six groups: (1) Control, (2) Control + NIR, (3) ZnO$_2$, (4) CZ, (5) CZP, and (6) CZP + NIR and received correspond treatment (Fig. 7a). Each group of mice received a total of four *i.t.* drug injections, and the NIR group was subjected to a single near-infrared laser irradiation on Day 0. As shown in Fig. 7b and c, the thermal imaging and the corresponding temperature-time curves revealed that the average temperature at the tumor site in the CZP + NIR treated mice reached 53.0 °C. In stark contrast, the temperature increase in the NIR group was quite limited, only reaching 38℃. This is attributed to the good tissue penetration of 808 nm near-infrared light, which is minimally absorbed by normal tissues. By administering CZP via *i.t.* injection, we achieved targeted photothermal therapy in the tumor tissue, minimizing thermal damage to surrounding normal tissues. On the first day after PTT, mice were injected with 4T1 cells subcutaneously on the contralateral dorsal region to establish a distant tumor model and keep them growing naturally. Tumor size and body weight were recorded every other day from day 0. The results showed that no statistically significant body weight changes were observed throughout treatments (Fig. 7d), suggesting minimal side effects of CZP NPs. Furthermore, mice treated with CZP + NIR exhibited the most effective tumor growth inhibition on day 12, with an average primary tumor volume of 111.2 mm^3, which was 22.0% of the Control group (506.2 mm^3), 20.3% of the Control + NIR group (548.5 mm^3), and 48.6% of the CZP group (228.6 mm^3), while the ZnO$_2$ (394.9 mm^3) and CZ (297.1 mm^3) groups showed limited tumor inhibitory effects (Fig. 7e and Fig. S21). The tumor weights (Fig. 7f) and corresponding photographs (Fig. 7g, left) further substantiated these findings. Lastly, we analyzed the formation rate of distant tumors in each group. As shown in Fig. 7g (right), mice treated with CZP + NIR showed effective resistance to distant tumor formation, confirming that CZP + NIR treatment can induce a sustained antitumor immune response, effectively inhibiting the growth of metastatic tumors at distant sites.

CZP reprogrammed the tumor immune microenvironment in vivo

As previously discussed, CZP NPs can effectively activate the cGAS-STING pathway through PTT combined with cuproptosis, leading to the release of type I interferons that promote the maturation of DCs within tumor-draining lymph nodes (TDLNs). Thus, we utilized flow cytometry to analyze the maturation of DCs in TDLNs of mice across various treatment groups. The results revealed that the proportion of mature DCs ($CD11c^+CD80^+CD86^+$) in TDLNs from mice treated with CZP + NIR was approximately 37.6% (Fig. 7h and i), which is 1.3 times higher than that observed in Control (29.4%) and Control + NIR groups (30.0%), suggesting that the combined CZP + NIR therapy can significantly enhance DCs maturation. Given that mature DCs are pivotal in presenting antigens to T cells, thereby initiating tumor-specific adaptive immune responses, we evaluated the infiltration of T cells within tumors. Notably, mice treated with CZP + NIR exhibited the highest infiltration of $CD3^+CD8^+$ cytotoxic T cells (61.4%), which is 1.9 times and 1.6 times greater than that of the Control (32.6%) and Control + NIR groups (39.2%), respectively (Fig. 7j and k). Furthermore, we observed a significant reduction in the ratio of immunosuppressive regulatory T cells (Tregs, $CD4^+CD25^+Foxp3^+$) in the CZP + NIR group relative to other treatment groups (Fig. 7l and m). The CZP + NIR treatment also markedly restricted the presence of immunosuppressive M2-like tumor-associated macrophages (TAMs, $CD11b^+F4/80^+CD206^+$) (Fig. 7n and o). Immunofluorescence staining results further substantiated these findings, showing a pronounced increase in $CD8^+$ T cell infiltration within tumor tissues following CZP + NIR treatment (Fig. 7p and Fig. S22). Moreover, the result of TUNEL staining confirmed that the green fluorescence intensity (indicating DNA damage) in tumor tissues of mice treated with CZP + NIR was the most intense. H&E staining also indicated the most severe tumor necrosis in the CZP + NIR treated group compared to others, demonstrating its potent antitumor effect (Fig. 7p). In summary, these findings demonstrate that the CZP + NIR treatment can effectively induce systemic antitumor immune responses by activating the cGAS-STING pathway, enhancing the recruitment of cytotoxic T lymphocytes and reprogramming the immunosuppressive TME.

Assessment of lung metastasis inhibition

To thoroughly assess the ability of CZP + NIR treatment to suppress distant metastasis induced by a systemic antitumor immune response, we established a mouse model of whole-body metastasis. Initially, the establishment of the 4T1 orthotopic breast cancer model and the treatment protocol followed the methods detailed previously, with the sole modification of injecting 4T1-luc cells intravenously on day 1 to simulate malignant tumor invasion and hematogenous spread (Fig. S23). Tumor cells entering the bloodstream can infiltrate various organs, with a particular propensity for the lungs. On day 12, D-luciferin potassium salt was administered intraperitoneally to each group of mice, followed by the assessment of fluorescence intensity using the IVIS to evaluate tumor metastasis. The results indicated extensive tumor metastasis in both the Control and Control + NIR groups, with fluorescence intensities in the lungs of 1.28×10^7 p/s and 1.39×10^7 p/s, respectively (Fig. S24). While treatments with various nanoparticles have moderately diminished distant metastasis, the CZP and CZP + NIR treatments were the most potent, significantly lowering lung fluorescence intensities to 6.55×10^5 p/s and 7.24×10^5 p/s, respectively. Moreover, H&E staining confirmed that CZP + NIR treatment resulted in the fewest lung metastatic nodules among all groups (Fig. S25), signifying a potent suppression of lung metastasis.

CZP combined with αPD-L1 synergistically enhanced antitumor efficacy

Having confirmed that CZP + NIR treatment robustly stimulates antitumor immunity, we evaluated the antineoplastic effects of CZP + NIR in combination with αPD-L1 in vivo (Fig. 8a). Our preliminary findings have established that CZP NPs can significantly upregulate PD-L1 expression in tumors, pointing to a potential synergistic enhancement when combined with αPD-L1. As depicted in Fig. 8b, no significant changes in body weight were observed during the treatment. The mice treated with CZP + NIR + αPD-L1 showed the most pronounced tumor growth inhibition, with an average tumor volume of 75.2 mm^3 on day 12 (Fig. 8c and Fig. S26). In contrast, the Control, αPD-L1, and CZP + NIR groups recorded average volumes of 630.5 mm^3, 490.0 mm^3, and 220.9 mm^3, respectively. Furthermore, the CZP + NIR + αPD-L1 treatment resulted in a markedly reduced average tumor weight of 0.11 g, which was significantly lower compared to the Control (0.80 g), αPD-L1 (0.71 g), and CZP + NIR (0.29 g) groups (Fig. 8d). These results suggest that our combinatorial CZP + NIR + αPD-L1 strategy is more effective at inhibiting tumor growth than monotherapy.

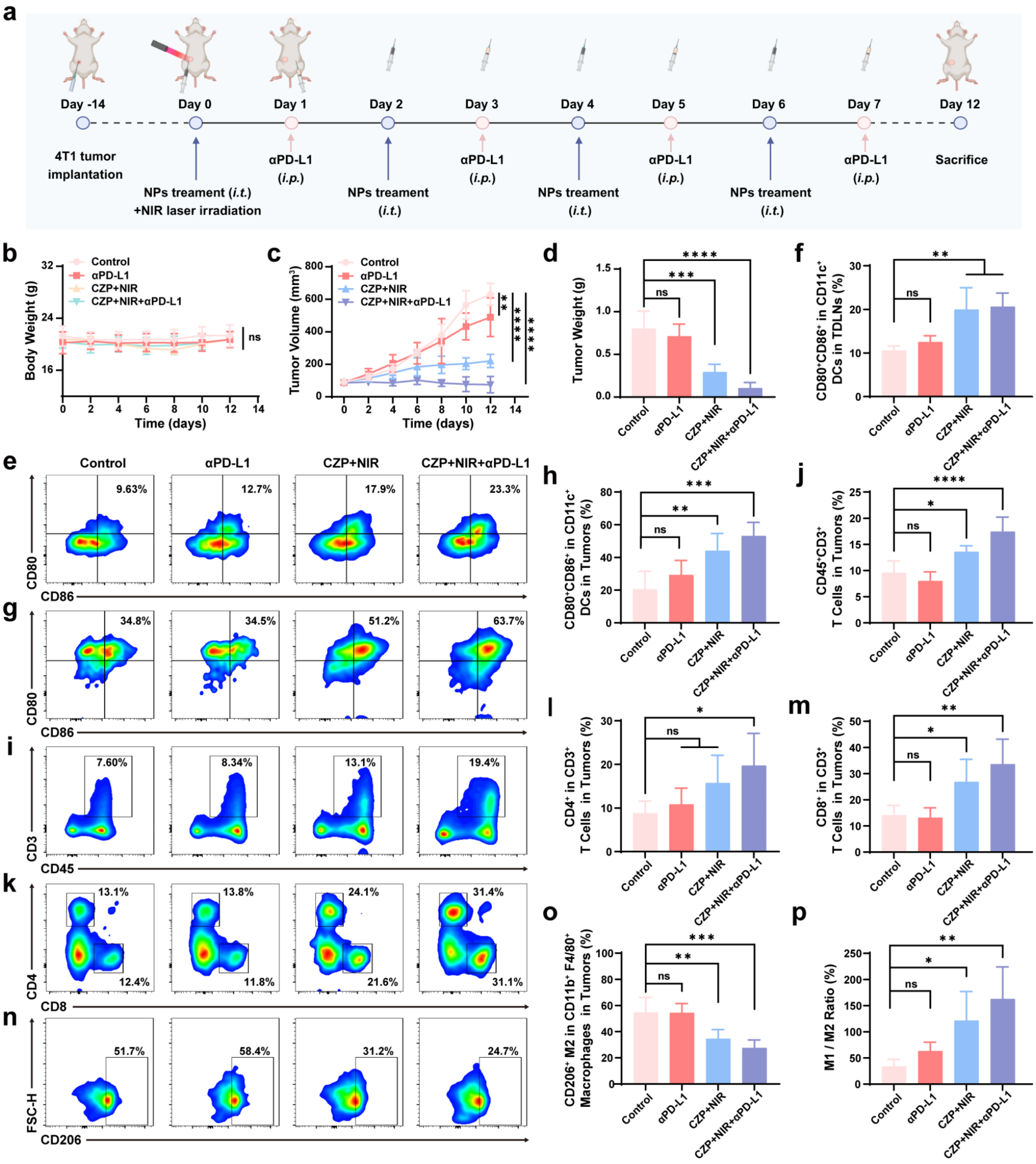

Fig. 8 Immune activation and antitumor effect of CZP NPs combined with αPD-L1 in vivo. **(a)** Schematic illustration of the experimental schedule for 4T1 tumor-bearing mice. **(b)** Body weights, **(c)** Tumor growth curves, and **(d)** tumor weights of 4T1 tumor-bearing mice after various treatment ($n=5$). Representative flow cytometry plots and corresponding quantifications of **(e**, **f)** mature DCs in TDLNs ($n=4$), **(g**, **h)** mature DCs in tumors, **(i**, **j)** $CD3^+$ T cells, **(k-m)** $CD3^+CD4^+$, $CD3^+CD8^+$ T cells and **(n**, **o)** M2 phenotype tumor-associated macrophages in tumors from mice following various treatments ($n=5$). **(p)** Analysis of the M1/M2 ratio variations

For further analysis, TDLNs and tumor tissues from the mice across all treatment groups were harvested for a comprehensive analysis of the TME. Specifically, in the CZP + NIR + αPD-L1 group, the proportion of mature DCs in TDLNs significantly rose to 20.7% (Fig. 8e and f), 1.95 times higher than the Control group (10.6%). Consistent with this, a similar increase in mature DCs was also observed within the tumor tissues (Fig. 8g and h). Moreover, The CZP + NIR + αPD-L1 treatment resulted in a significant increase in the tumoral infiltration of CD3$^+$ T cells, CD3$^+$CD4$^+$ T cells, and CD3$^+$ CD8$^+$ T cells, with respective percentages elevated to 17.4%, 19.7%, and 33.6%, all notably higher than those observed in other groups (Fig. 8i-m). Concurrently, this combined therapy also elevated the proportion of pro-inflammatory M1-like TAMs (CD11b$^+$F4/80$^+$CD86$^+$) while decreasing the proportion of anti-inflammatory M2-like TAMs (CD11b$^+$F4/80$^+$CD206$^+$) (Fig. 8n, o and Fig. S27), which resulted in a dramatic increase in the M1/M2 ratio, rising sharply from 33.9% in the Control group to 162.7% (Fig. 8p). In conclusion, the combined CZP + NIR + αPD-L1 therapy effectively remodels the immunosuppressive TME, triggering a potent antitumor immune response.

Conclusion

In summary, we constructed polydopamine (PDA)-coated zinc-copper bimetallic nanoplatforms (CZP NPs) for linking PTT, cuproptosis, cGAS-STING activation and immunotherapy in TNBC. CZP NPs can rapidly elevating intracellular ROS levels, inducing cuproptosis, and causing the release of mtDNA. Furthermore, CZP NPs effectively promotes the maturation of DCs and the infiltration of cytotoxic CD8$^+$ T cells into the tumor *via* activating cGAS-STING signaling pathway, thereby converting ‘cold’ TME into immunologically ‘hot’ TME. Additionally, the integration of PTT serves to amplify cuproptosis and cGAS-STING activation, further enhancing the therapeutic impact. Moreover, we demonstrated that CZP NPs enhances the responsiveness of tumor cells to αPD-L1 treatment by upregulating the expression of PD-L1 effectively. In vivo evidence confirms that a strategic combination of CZP NPs with αPD-L1 can significantly improve the therapeutic effect against TNBC by promoting DCs maturation, cytotoxic CD8$^+$ T cell infiltration, and M1 polarization in tumors, ultimately inhibiting TNBC growth and metastasis. These effects suggest significant clinical application potential. However, the clinical translation of nanomaterials still faces numerous challenges. Firstly, although CZP NPs have shown good biosafety in animal model, differences between human and animal physiology and metabolic pathways mean that their long-term safety and potential toxicity in humans require further investigation. Additionally, the shape, size, and surface modification of nanoparticles can significantly impact their distribution within the human body. Further modification of CZP NPs to enhance targeted delivery to tumor tissues could improve therapeutic outcomes. Moreover, the variability in individual immune responses may lead to different responses to the same treatment strategy. Therefore, personalized treatment plans tailored to individual patients can help achieve more stable therapeutic outcomes. Collectively, our study presents a promising strategy employing zinc-copper bimetallic nanoplatforms to amplify cuproptosis and cGAS-STING activation for enhancing TNBC immunotherapy.

Supplementary Information

The online version contains supplementary material available at https://doi.org/10.1186/s12951-025-03186-4.

Supplementary Material 1

Acknowledgements

Some figures in this work were created in BioRender.com.

Author contributions

B.Z., M.C., and Z.H. contributed equally to this work. B.Z.: Writing– original draft, Conceptualization, Investigation. M.C.: Methodology, Investigation. Z.H.: Methodology, Investigation. L.L.: Formal analysis, Investigation, Funding acquisition. Y.Z.: Investigation, Methodology. B.F.: Investigation. M.S.: Investigation. G.R.: Validation, Methodology. K.W.: Methodology. H.L.: Investigation. J.Z.: Software. X.Z.: Methodology. S.Y.: Investigation. I.S.: Methodology. J.Z.: Methodology. J.H.: Funding acquisition, Supervision. Z.Y.: Writing– review & editing, Supervision, Conceptualization. F.Q.: Writing– review & editing, Supervision, Project administration, Funding acquisition, Conceptualization. All authors have discussed the results and approved the final manuscript.

Funding

This research was financially supported by the National Natural Science Foundation of China (82273268, 81930079, 82302901), Key research and development program of Zhejiang Province (2025C01105), and China Postdoctoral Science Foundation Grant (2023M74301).

Data availability

RNA-sequencing data supporting this study’s findings have been deposited into the NCBI Sequence Read Archive (SRA: PRJNA1171492). All data are available from the corresponding author on reasonable request.

Declarations

Ethics approval and consent to participate

All animal experiments were conducted following the protocols approved by the Ethics Committee of Zhejiang Chinese Medical University (ACUC-20220530-09). All participants consented to publish the paper.

Consent for publication

Not applicable.

Competing interests

The authors declare no competing interests.

Author details

[1]Key Laboratory of Tumor Microenvironment and Immune Therapy of Zhejiang Province, The Second Affiliated Hospital, Zhejiang University School of Medicine, Hangzhou 310009, P.R. China

[2]Department of Medical Oncology, The Second Affiliated Hospital, Zhejiang University School of Medicine, Hangzhou 310009, P.R. China

[3]Laboratory of Nanomedicine, Medical Science Research Center, School of Medicine, Shaoxing University, Shaoxing 312000, Zhejiang Province, P. R. China
[4]Department of Breast Surgery, The Second Affiliated Hospital, Zhejiang University School of Medicine, Hangzhou 310009, P.R. China

Received: 25 November 2024 / Accepted: 1 February 2025

References

1. Siegel RL, Giaquinto AN, Jemal A. Cancer statistics, 2024. Ca-Cancer J Clin. 2024;74(1):12–49.
2. Won KA, Spruck C. Triple–negative breast cancer therapy: current and future perspectives (review). Int J Oncol. 2020;57(6):1245–61.
3. Garrido-Castro AC, Lin NU, Polyak K. Insights into Molecular classifications of Triple-negative breast Cancer: improving patient selection for treatment. Cancer Discov. 2019;9(2):176–98.
4. Dent R, Trudeau M, Pritchard KI, Hanna WM, Kahn HK, Sawka CA, et al. Triple-negative breast cancer: clinical features and patterns of recurrence. Clin Cancer Res. 2007;13(15 Pt 1):4429–34.
5. Riley RS, June CH, Langer R, Mitchell MJ. Delivery technologies for cancer immunotherapy. Nat Rev Drug Discovery. 2019;18(3):175–96.
6. Topalian SL, Forde PM, Emens LA, Yarchoan M, Smith KN, Pardoll DM. Neoadjuvant immune checkpoint blockade: a window of opportunity to advance cancer immunotherapy. Cancer Cell. 2023;41(9):1551–66.
7. Liu D, Schilling B, Liu D, Sucker A, Livingstone E, Jerby-Arnon L, et al. Integrative molecular and clinical modeling of clinical outcomes to PD1 blockade in patients with metastatic melanoma. Nat Med. 2019;25(12):1916–27.
8. Robert C, Schachter J, Long GV, Arance A, Grob JJ, Mortier L, et al. Pembrolizumab versus Ipilimumab in Advanced Melanoma. N Engl J Med. 2015;372(26):2521–32.
9. Gadgeel S, Rodríguez-Abreu D, Speranza G, Esteban E, Felip E, Dómine M, et al. Updated analysis from KEYNOTE-189: Pembrolizumab or Placebo Plus Pemetrexed and Platinum for previously untreated metastatic nonsquamous non-small-cell Lung Cancer. J Clin Oncol. 2020;38(14):1505–17.
10. Galon J, Bruni D. Approaches to treat immune hot, altered and cold tumours with combination immunotherapies. Nat Rev Drug Discovery. 2019;18(3):197–218.
11. Taifour T, Attalla SS, Zuo D, Gu Y, Sanguin-Gendreau V, Proud H, et al. The tumor-derived cytokine Chi3l1 induces neutrophil extracellular traps that promote T cell exclusion in triple-negative breast cancer. Immunity. 2023;56(12):2755–e27728.
12. Timperi E, Gueguen P, Molgora M, Magagna I, Kieffer Y, Lopez-Lastra S, et al. Lipid-Associated macrophages Are Induced by Cancer-Associated fibroblasts and mediate Immune suppression in breast Cancer. Cancer Res. 2022;82(18):3291–306.
13. Mittendorf EA, Philips AV, Meric-Bernstam F, Qiao N, Wu Y, Harrington S, et al. PD-L1 expression in triple-negative breast cancer. Cancer Immunol Res. 2014;2(4):361–70.
14. Miles D, Gligorov J, André F, Cameron D, Schneeweiss A, Barrios C, et al. Primary results from IMpassion131, a double-blind, placebo-controlled, randomised phase III trial of first-line paclitaxel with or without atezolizumab for unresectable locally advanced/metastatic triple-negative breast cancer. Ann Oncol. 2021;32(8):994–1004.
15. van den Berghe PV, Klomp LW. New developments in the regulation of intestinal copper absorption. Nutr Rev. 2009;67(11):658–72.
16. Turski ML, Thiele DJ. New roles for copper metabolism in cell proliferation, signaling, and disease. J Biol Chem. 2009;284(2):717–21.
17. Guo H, Wang Y, Cui H, Ouyang Y, Yang T, Liu C, et al. Copper induces spleen damage through modulation of oxidative stress, apoptosis, DNA damage, and inflammation. Biol Trace Elem Res. 2022;200(2):669–77.
18. Banci L, Bertini I, Ciofi-Baffoni S, Kozyreva T, Zovo K, Palumaa P. Affinity gradients drive copper to cellular destinations. Nature. 2010;465(7298):645–8.
19. Chen L, Min J, Wang F. Copper homeostasis and cuproptosis in health and disease. Signal Transduct Target Ther. 2022;7(1):378.
20. Tsvetkov P, Coy S, Petrova B, Dreishpoon M, Verma A, Abdusamad M, et al. Copper induces cell death by targeting lipoylated TCA cycle proteins. Science. 2022;375(6586):1254–61.
21. Huang L, Zhu J, Xiong W, Feng J, Yang J, Lu X, et al. Tumor-generated reactive oxygen species storm for high-performance ferroptosis therapy. ACS Nano. 2023;17(12):11492–506.
22. Wang Z, Ren X, Li Y, Qiu L, Wang D, Liu A, et al. Reactive oxygen species amplifier for apoptosis-ferroptosis mediated high-efficiency radiosensitization of tumors. ACS Nano. 2024;18(14):10288–301.
23. Lu J, Jiang Z, Ren J, Zhang W, Li P, Chen Z, et al. One-Pot synthesis of multifunctional Carbon-based nanoparticle-supported dispersed Cu(2+) disrupts Redox Homeostasis to Enhance CDT. Angew Chem Int Ed Engl. 2022;61(4):e202114373.
24. Yu X, Li B, Yan J, Li W, Tian H, Wang G, et al. Cuproptotic nanoinducer-driven proteotoxic stress potentiates cancer immunotherapy by activating the mtDNA-cGAS-STING signaling. Biomaterials. 2024;307:122512.
25. Cen D, Ge Q, Xie C, Zheng Q, Guo J, Zhang Y, et al. ZnS@BSA Nanoclusters Potentiate Efficacy of Cancer Immunotherapy. Adv Mater. 2021;33(49):e2104037.
26. Tang W, Wu J, Wang L, Wei K, Pei Z, Gong F, et al. Bioactive layered double hydroxides for synergistic Sonodynamic/Cuproptosis Anticancer Therapy with Elicitation of the Immune response. ACS Nano. 2024;18(15):10495–508.
27. Guo B, Yang F, Zhang L, Zhao Q, Wang W, Yin L, et al. Cuproptosis Induced by ROS responsive nanoparticles with Elesclomol and Copper Combined with αPD-L1 for enhanced Cancer Immunotherapy. Adv Mater. 2023;35(22):e2212267.
28. Lu S, Li Y, Yu Y. Glutathione-scavenging Celastrol-Cu nanoparticles induce self-amplified cuproptosis for Augmented Cancer Immunotherapy. Adv Mater. 2024;36(35):e2404971.
29. Zheng P, Zhou C, Lu L, Liu B, Ding Y. Elesclomol: a copper ionophore targeting mitochondrial metabolism for cancer therapy. J Exp Clin Cancer Res. 2022;41(1):271.
30. Jiang M, Chen P, Wang L, Li W, Chen B, Liu Y, et al. cGAS-STING, an important pathway in cancer immunotherapy. J Hematol Oncol. 2020;13(1):81.
31. Corrales L, Gajewski TF. Molecular pathways: targeting the stimulator of Interferon genes (STING) in the Immunotherapy of Cancer. Clin Cancer Res. 2015;21(21):4774–9.
32. Wang H, Hu S, Chen X, Shi H, Chen C, Sun L, et al. cGAS is essential for the antitumor effect of immune checkpoint blockade. Proc Natl Acad Sci U S A. 2017;114(7):1637–42.
33. Ablasser A, Goldeck M, Cavlar T, Deimling T, Witte G, Röhl I, et al. cGAS produces a 2′-5′-linked cyclic dinucleotide second messenger that activates STING. Nature. 2013;498(7454):380–4.
34. Chin EN, Yu C, Vartabedian VF, Jia Y, Kumar M, Gamo AM, et al. Antitumor activity of a systemic STING-activating non-nucleotide cGAMP mimetic. Science. 2020;369(6506):993–9.
35. Glück S, Guey B, Gulen MF, Wolter K, Kang TW, Schmacke NA, et al. Innate immune sensing of cytosolic chromatin fragments through cGAS promotes senescence. Nat Cell Biol. 2017;19(9):1061–70.
36. Wang X, Liu Y, Xue C, Hu Y, Zhao Y, Cai K, et al. A protein-based cGAS-STING nanoagonist enhances T cell-mediated anti-tumor immune responses. Nat Commun. 2022;13(1):5685.
37. Victorelli S, Salmonowicz H, Chapman J, Martini H, Vizioli MG, Riley JS, et al. Apoptotic stress causes mtDNA release during senescence and drives the SASP. Nature. 2023;622(7983):627–36.
38. West AP, Shadel GS. Mitochondrial DNA in innate immune responses and inflammatory pathology. Nat Rev Immunol. 2017;17(6):363–75.
39. Chen Q, Sun L, Chen ZJ. Regulation and function of the cGAS-STING pathway of cytosolic DNA sensing. Nat Immunol. 2016;17(10):1142–9.
40. Byun JK, Park M, Lee S, Yun JW, Lee J, Kim JS, et al. Inhibition of glutamine utilization synergizes with Immune checkpoint inhibitor to promote Antitumor Immunity. Mol Cell. 2020;80(4):592–e6068.
41. Jin X, Ding D, Yan Y, Li H, Wang B, Ma L, et al. Phosphorylated RB promotes Cancer immunity by inhibiting NF-κB activation and PD-L1 expression. Mol Cell. 2019;73(1):22–e356.
42. Vasiyani H, Mane M, Rana K, Shinde A, Roy M, Singh J, et al. DNA damage induces STING mediated IL-6-STAT3 survival pathway in triple-negative breast cancer cells and decreased survival of breast cancer patients. Apoptosis. 2022;27(11–12):961–78.
43. Xu L, Peng F, Luo Q, Ding Y, Yuan F, Zheng L, et al. IRE1α silences dsRNA to prevent taxane-induced pyroptosis in triple-negative breast cancer. Cell. 2024;187(25):7248-7266.e34.
44. Fu J, Kanne DB, Leong M, Glickman LH, McWhirter SM, Lemmens E, et al. STING agonist formulated cancer vaccines can cure established tumors resistant to PD-1 blockade. Sci Transl Med. 2015;7(283):283ra52.

45. Du M, Chen ZJ. DNA-induced liquid phase condensation of cGAS activates innate immune signaling. Science. 2018;361(6403):704–9.
46. Hu W, Zhen W, Zhang M, Wang W, Jia X, An S, et al. Development of Nickel Selenide@polydopamine nanocomposites for magnetic resonance imaging guided NIR-II Photothermal Therapy. Adv Healthc Mater. 2021;10(23):e2101542.
47. Lin LS, Huang T, Song J, Ou XY, Wang Z, Deng H, et al. Synthesis of copper peroxide nanodots for H(2)O(2) self-supplying Chemodynamic Therapy. J Am Chem Soc. 2019;141(25):9937–45.
48. Fu LH, Wan Y, Qi C, He J, Li C, Yang C, et al. Nanocatalytic theranostics with glutathione depletion and enhanced reactive oxygen species generation for efficient Cancer therapy. Adv Mater. 2021;33(7):e2006892.
49. Koo S, Park OK, Kim J, Han SI, Yoo TY, Lee N, et al. Enhanced chemodynamic therapy by Cu-Fe Peroxide nanoparticles: Tumor microenvironment-mediated synergistic Fenton Reaction. ACS Nano. 2022;16(2):2535–45.
50. Ding T, Wang Z, Xia D, Zhu J, Huang J, Xing Y et al. Long-lasting reactive Oxygen species Generation by Porous Redox Mediator-Potentiated Nanoreactor for Effective Tumor Therapy. Adv Funct Mater. 2021;31(13).
51. Xie J, Yang Y, Gao Y, He J. Cuproptosis: mechanisms and links with cancers. Mol Cancer. 2023;22(1):46.
52. Zorov DB, Juhaszova M, Sollott SJ. Mitochondrial reactive oxygen species (ROS) and ROS-induced ROS release. Physiol Rev. 2014;94(3):909–50.

Publisher's note